



Available online at www.keaipublishing.com/en/journals/journal-of-magnesium-and-alloys/

ScienceDirect

Journal of Magnesium and Alloys 13 (2025) 3725-3739



www.elsevier.com/locate/jma

Full Length Article

Research on strength-ductility and fracture behavior of ultra-fine bio-magnesium alloys via double-sided friction stir processing using liquid CO₂ cooling th

Kun Sheng^{a,b,d}, Shaokang Guan^{b,c,*}, Yufeng Sun^b, Yoshiaki Morisada^d, Hidetoshi Fujii^{d,**}

^a Institute for Genetic Engineering of Materials, Henan Academy of Sciences, Zhengzhou 450046, China
^b School of Materials Science and Engineering & Henan Key Laboratory of Advanced Magnesium Alloys, Zhengzhou University, Zhengzhou 450001, China
^c Key Laboratory of Advanced Materials Processing & Mold Ministry of Education, Zhengzhou 450002, China
^d Joining and Welding Research Institute (JWRI), Osaka University, Osaka 567-0047, Japan

Received 25 November 2024; received in revised form 12 February 2025; accepted 19 February 2025 Available online 1 April 2025

Abstract

Bio-magnesium (Mg) alloys exhibit excellent biocompatibility and biodegradability, making them highly promising for implant applications. However, their limited strength-ductility balance remains a critical challenge restricting widespread use. In this study, ultra-fine-grained and homogeneous Mg alloys were fabricated using double-sided friction stir processing (DS-FSP) with liquid CO₂ rapid cooling, leading to a significant enhancement in the strength-ductility synergy of the stirred zone. The results demonstrate that DS-FSP samples exhibit simultaneous improvements in ultimate tensile strength (UTS) and elongation, reaching 334.1 ± 15 MPa and 28.2 ± 7.3%, respectively. Compared to the non-uniform fine-grained microstructure obtained through single-sided friction stir processing, DS-FSP generates a uniform ultra-fine-grained structure, fundamentally altering the fracture behavior and mechanisms of Mg alloys. The DS-FSP samples exhibit irregular fracture patterns due to variations in basal slip system activation among different grains. In contrast, single-sided friction stir processing samples, characterized by a fine-grained yet heterogeneous microstructure, display flat shear fractures dominated by high-density dislocation initiation induced by twin formation, with fracture propagation dictated by the non-uniform texture. By achieving an ultra-fine grain size and homogeneous texture, DS-FSP effectively modifies the fracture mechanisms, thereby enhancing the strength-ductility balance of bio-magnesium alloys.

© 2025 Chongqing University. Publishing services provided by Elsevier B.V. on behalf of KeAi Communications Co. Ltd.

This is an open access article under the CC BY-NC-ND license (http://creativecommons.org/licenses/by-nc-nd/4.0/)

Keywords: Bio-magnesium alloys; Double-sided friction stir processing; Homogeneous microstructure; Ultra-fine grain; Strength-ductility; Fracture behavior.

1. Introduction

Bio-magnesium alloys, known for their bio-compatibility and biodegradability, are emerging as promising alternatives to traditional orthopedic and bio-material implants [1–3]. However, the inherent crystal structure of magnesium alloys presents significant challenges, including limited strength-ductility and hindered formability, which restrict their broader

E-mail addresses: skguan@zzu.edu.cn (S. Guan), fujii.hidetoshi.jwri@osaka-u.ac.jp (H. Fujii).

application [4–6]. Grain refinement, particularly through the development of ultra-fine grains, has proven to be a valuable strategy for overcoming these limitations, with Severe Plastic Deformation (SPD) being a common method to achieve ultra-fine-grained structures in Mg alloys [7–9]. Widely used SPD techniques include extrusion [2,10–15], rolling [16,17], and friction stir processing (FSP) [18–22]. Numerous studies demonstrate that Mg alloys with ultra-fine grains processed through SPD exhibit enhanced strength-ductility properties [7–9]. For instance, Zhao et al. achieved ultra-fine grains in Mg-3Al-1Zn-0.2Mn through extrusion, resulting in a UTS of 332.08 MPa and an elongation of 16.9% [7]. Similarly, Klu et al. produced Mg-9Li-1Al plates with ultra-fine grains and excellent mechanical properties through a combination of ex-

[☆] Peer review under the responsibility of Chongqing University.

^{*} Corresponding author: School of Materials Science and Engineering, Zhengzhou University, Zhengzhou, 450001, China.

^{**} Corresponding author.

trusion and repeated rolling, achieving a UTS of 312 MPa and an elongation of 20% [9]. Recent advancements in FSP, particularly the friction stir vibration process (FSVP), have shown significant promise in further improving the mechanical properties of magnesium alloys. FSVP modifies traditional FSP by introducing vibration, which enhances microstructure refinement, strength, and ductility. Studies on AZ91 magnesium alloy composites reinforced with SiC nanoparticles have highlighted the benefits of FSVP in achieving these improvements [23–26].

Despite the success of SPD in grain refinement, samples produced by these methods are often limited in size, restricting their applicability. In contrast, FSP is particularly advantageous due to its ability to induce high strain without additional heating, allowing for the efficient processing of larger samples. FSP works by applying substantial loads and tool rotation, inducing shear deformation that refines the microstructure [21,22,27]. However, the ductility of Mg alloys processed by FSP remains limited. For example, Nasiri et al. observed that, despite refining the grain size to 1.7 µm, the UTS of ascast samples increased from 157 MPa to 267.2 MPa, while the elongation showed only a modest increase from 2% to 10% [28]. This limited ductility is attributed to insufficient material plastic flow in the root of the stir zone (SZ), resulting in micro-porous defects [29]. Jia et al. further noted that the steep temperature gradient in FSP causes interrupted material flow, leading to void defects [30]. To address these issues, multi-pass one-sided FSP (MFSP) has been proposed. Elyasi et al. demonstrated that MFSP significantly improved the UTS and elongation of Mg alloys by up to 90% and 566%, respectively [31]. However, the accumulation of defects during MFSP may negatively impact ductility, and some researchers have attributed this low ductility to the heterogeneous microstructure in the SZ, including grain size and texture [27,28]. Park et al. reported that the texture in the stirred region of one-sided FSP samples is highly heterogeneous, with a strong accumulation of the {0001} basal plane texture on the top surface, causing premature fractures at these locations [32]. Understanding the factors that govern fracture behavior in FSP-processed Mg alloys is essential for further improving their strength-ductility.

DS-FSP offers a potential solution to these challenges. By providing more complex material flows and further refining the grain structure, DS-FSP helps avoid the heterogeneous microstructure typically observed in one-sided FSP samples. For instance, Yang et al. demonstrated that DS-FSP of 7050-T7451 aluminum alloy plates improved the uniformity of micro-hardness distribution in the SZ [33], while Raturi et al. found that DS-FSP of AA6061-AA7075 aluminum alloys led to the lowest susceptibility to corrosion, attributed to the dissolution and decomposition of precipitated phases [34].

This study focuses on achieving ultra-fine grain biomagnesium alloys with a homogeneous microstructure and enhanced strength-ductility through DS-FSP combined with liquid CO₂ cooling. By analyzing the microstructure and fracture behavior of both one-sided FSP and DS-FSP samples,

this research contributes to a deeper understanding of the complex relationship between microstructure and mechanical performance, paving the way for enhanced strength-ductility in FSP-processed Mg alloys.

2. Experimental procedure

In this work, the bio-magnesium alloys (Mg-2wt%Zn-0.46wt%Y-0.5wt%Nd, abbr. ZE21B) plates were homogenized at 420 °C for 72 h. The homogenized alloys demonstrate a microstructure consisting of equiaxed grains, and the average grain size is $112\pm28~\mu m$, as illustrated in Fig. 1(a-b). From the scanning electron microscope (SEM) image obtained in secondary electron (SE) mode (Fig. 1c), the second-phase particles are dispersed inside the grains (indicated by the blue arrows) as well as along the grain boundaries (indicated by the red arrows). From X-ray diffraction (XRD) spectrum in Fig. 1d, the phases are α -Mg matrix, Mg_{6.8}Zn_{0.5}Y_{2.81} and NdZn₅ intermetallic compounds.

The detailed dimension of Mg alloys plates was shown in Fig. 2a. The Mg alloys plates underwent FSP using two processing methods: (I) MFSP, where two FSP passes were overlapped entirely on the same side A, and (II) DS-FSP, involving the initial FSP pass on side A and the subsequent pass on side B, as illustrated in Fig. 2a and 2b. The rotation speed was 600 rpm, while the processing speed was 100 mm⋅min⁻¹. The processing were cooled by liquid carbon dioxide. The tool was made of cemented carbide. These processing parameters were selected based on preliminary tests and literature guidelines to optimize the material's mechanical properties while maintaining process stability. The size of tool was shown in Fig. 2c. Tensile testing were conducted at the central regions of the SZ, as illustrated in Fig. 2d, and the size of tensile testing sample in Fig. 2e. The tensile velocity was $0.2 \text{ mm} \cdot \text{min}^{-1}$.

The specimen was finely polished using sandpaper and polishing reagents, followed by thorough cleaning with ethanol. For electron back-scattered diffraction (EBSD), the sample was further polished to a mirror finish using diamond paste, followed by electropolishing to remove any deformation layers. The step size used for EBSD data acquisition was 0.1 μm . The high-angle grain boundaries (HAGBs) were defined as boundaries with an angle greater than 15°, while low-angle grain boundaries (LAGBs) were identified with angles <15°. A Confidence Index (CI) of 2 was used to ensure the reliability of the EBSD results.

The stir zone (SZ) of MFSP and DS-FSP was characterized by optical microscopy (Olympus, BM-51X). The microstructure was further analyzed using scanning electron microscopy (SEM, JEOL-7001F), electron back-scattered diffraction (EBSD, JEOL-7001F), Transmission Electron Microscopy (TEM, JEOL JEM-2010), and X-ray diffraction (XRD, Bruker D8 DISCOVER). For TEM, thin foils were prepared using focused ion beam (FIB) milling to achieve electron transparency. XRD analysis was performed at the center of the homogenized Mg alloy.

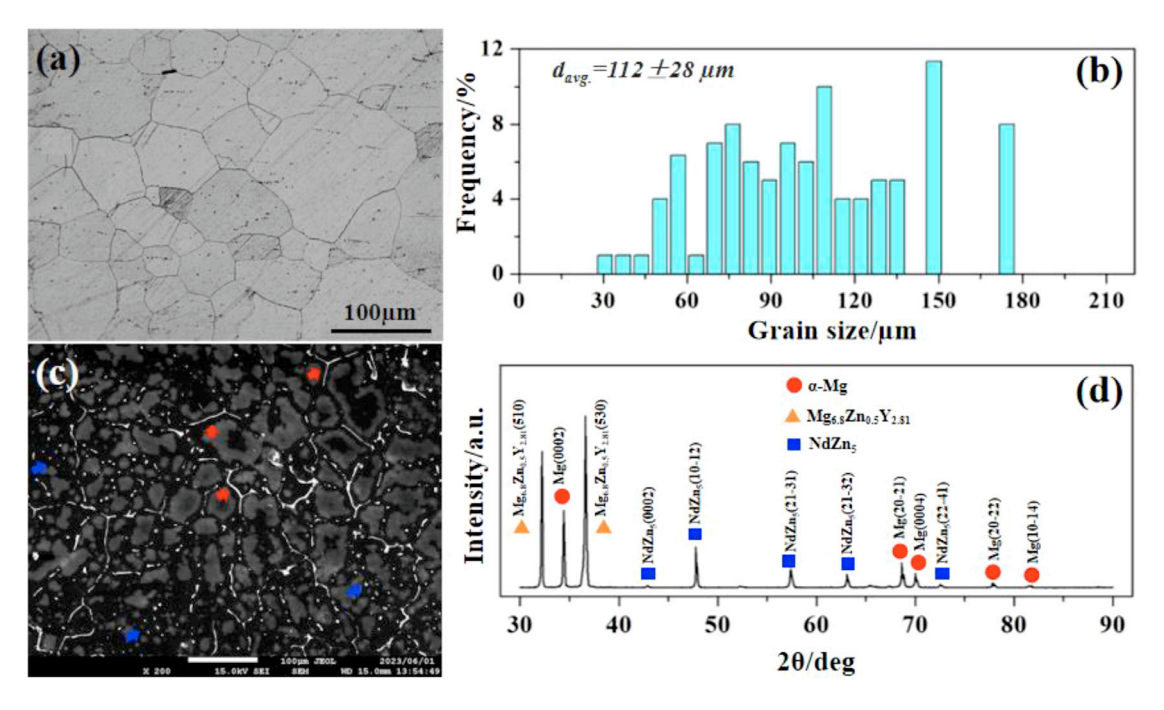


Fig. 1. The microstructural characteristics of homogenized alloys: (a) optical microscope image, (b) grain size distribution histogram, (c) SEM map and (d) XRD spectrum.

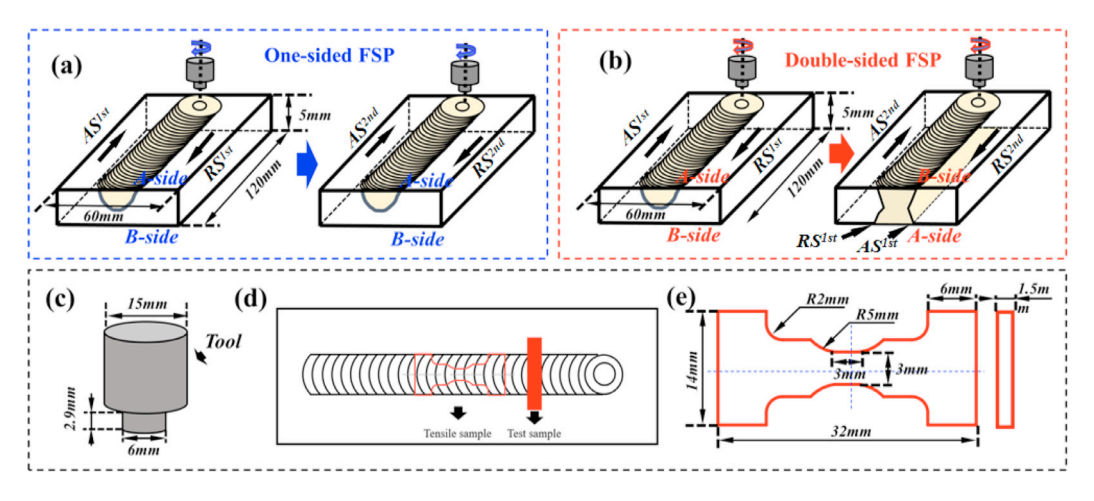


Fig. 2. (a) and (b) Schematic illustration MFSP and DS-FSP, (c) the size of tool, (d) the regions of tensile testing samples and experimental samples, (d) the size of tensile testing samples.

3. Results

The microstructural characteristics of the first pass FSP, MFSP, and DS-FSP samples are illustrated in Fig. 3, including the images in transverse cross sections, and the EBSD IPF maps. In this work, both the one pass FSP and the multipass one-sided FSP belong to one-sided FSP. From Fig. 3(a-c), there are no volumetric defects and micro-pores in the cross sections of all samples. For the one-sided FSP samples, the shapes closely resemble the shape of the tool, while the shape in DS-FSP sample presents dumbbell-shaped and shows higher symmetry in the SZ (highlighted by the red dashed lines). To further analyze the microstructural characteristics, some regions (as shown by the white rectangles) in the SZ are selected along the ND for the all samples, and regions

1, 2, and 3 (as shown by the white dots) are further selected within these regions. Through analyzing microstructural characteristics of the EBSD maps in Fig. 3(d-f), the following conclusions are obtained: (I) the microstructure of one-sided FSP samples (in Fig. 3(d-e)) is the fine-grained and heterogeneous, and the grain size increase from top zones to bottom zones, and (II) the microstructure of the DS-FSP sample, as shown in Fig. 3f, exhibits ultra-fine grains and a homogeneous texture. To minimize grain growth in region 1 due to thermal effects, we employed liquid CO₂ cooling throughout the friction stir process. This cooling method helps reduce the extent of grain growth and maintains the uniformity of the microstructure in the SZ. These results demonstrated that DS-FSP is beneficial to achieve ultra-fine grains and improve the uniformity of microstructure of the SZ.

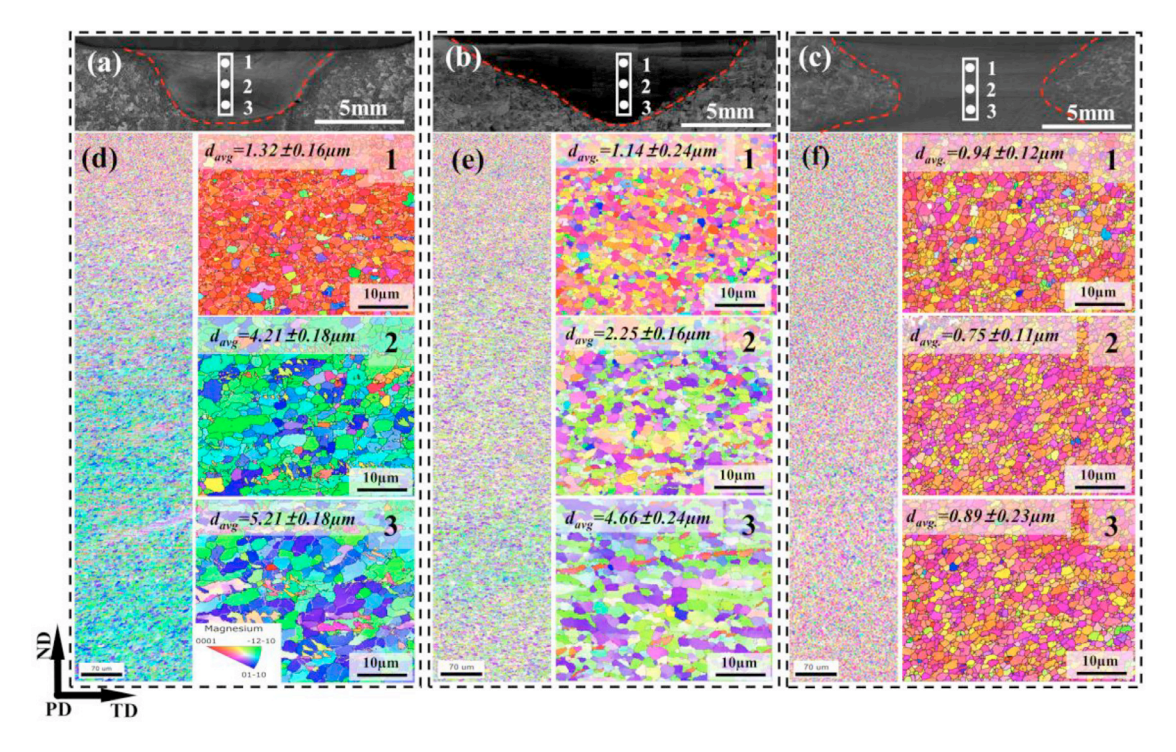


Fig. 3. The microstructural characteristics of the first pass FSP, MFSP and DS-FSP samples (both one pass FSP and MFSP belong to one-sided FSP): (a-c) images of transverse cross sections, (d-f) EBSD IPF maps of the SZ, where Fig. 3(d-f) are the white rectangle regions in Fig. 3(a-c) and EBSD IPF maps 1, 2 and 3 are the corresponding regions of white dots in each sample.

The {0001} pole figures of the first pass FSP, MFSP, and DS-FSP samples are presented in Fig. 4, corresponding to the EBSD IPF maps. The whole texture of the first pass FSP sample is {0001} \langle -1100 \rangle with the highest pole density of 59.27 mrd, and tilted to TD about 30°, as shown in Fig. 4a. Compared to the whole texture, the texture of the regions 1, 2 and 3 are tilted about 30°, 45° and 45° to TD, and the texture types are also quite different (in Fig. 4(b-d)), implying the existence of texture heterogeneity in the first pass FSP sample. Similarly, the whole texture (in Fig. 4e) of the MFSP sample is also {0001} \langle -1100 \rangle with the highest pole density of 60.59 mrd, and it is tilted to TD about 30°, but the texture of regions 1, 2 and 3 (in Fig. 4(f-h)) are tilted about 45°, 30° and 30° to TD.

The difference in grain orientation between the top and bottom regions of the stir zone in one-sided FSP samples is mainly due to thermal gradients, plastic deformation distribution, and cooling rate variations [29]. The top region, which is in direct contact with the tool shoulder, experiences higher temperatures, promoting more significant dynamic recrystallization, while the bottom region, being farther from the heat source, remains at a lower temperature, leading to differences in grain refinement [30]. Additionally, the top region undergoes more intense plastic deformation due to higher shear strain, whereas the bottom region experiences less deformation, affecting the crystallographic orientation. The cooling rate also differs, with the top cooling more slowly due to continuous heat input, allowing for prolonged recrystallization, while the bottom cools faster due to contact with the base material, limiting grain growth [31]. In MFSP, the second pass further alters the bottom region's microstructure, but initial differences in grain structure, strain hardening, and crystallographic orientation persist, and thermal accumulation may further modify the microstructure without completely eliminating these variations.

On the contrast, the texture of the DS-FSP sample is homogeneous both in whole and regions 1, 2 and 3, as shown in Fig. 4(i-1), and it is the silk texture parallel to TD. In addition, the maximum pole density in the SZ reached 10.11 mrd for the DS-FSP sample, indicating DS-FSP method reduces the anisotropy and density of texture, and this finding has also been documented by Liu et al. [29]. DS-FSP enhances microstructural homogeneity by mitigating strain gradients, optimizing thermal cycles, and promoting uniform dynamic recrystallization. Unlike single-pass FSP, where asymmetric material flow and localized deformation lead to microstructural anisotropy, DS-FSP subjects the material to two consecutive deformation and thermal cycles, resulting in a more balanced strain distribution across the SZ. The bidirectional stirring process refines the grain structure by facilitating more uniform dynamic recrystallization, reducing local variations in grain size and crystallographic orientation. Furthermore, DS-FSP promotes a more uniform heat distribution, minimizing temperature gradients and suppressing excessive grain growth in specific regions. This process also optimizes material flow, reducing localized inhomogeneities and enhancing textural uniformity. Consequently, DS-FSP decreases texture anisotropy and refines the overall microstructure, as evidenced by the reduced maximum pole density in the SZ. Additionally, in accordance with pertinent literatures, reduc-

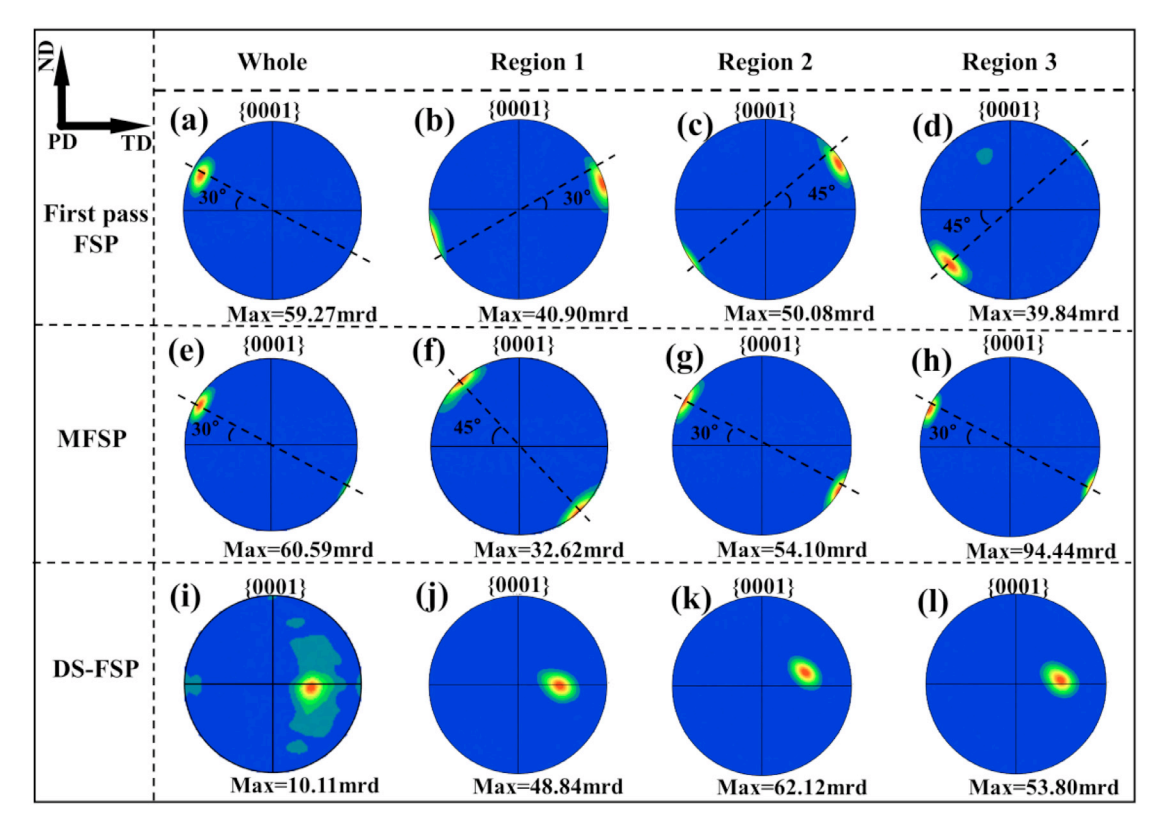


Fig. 4. The {0001} pole figures of the whole and typical regions (regions 1, 2 and 3): (a-d) the first pass FSP sample, (e-h) MFSP sample, (i-l) DS-FSP sample.

ing the anisotropy and density of texture promotes uniform plastic deformation and reduces local stress concentration, thereby enhancing strength-ductility of Mg alloys under stress [35–37].

Figs. 5 and 6 provide detailed insights into the distribution and refinement of intermetallic compounds (IMCs) in the SZ of the first pass FSP sample, MFSP sample and DS-FSP samples. As shown in Fig. 5(a-c), after the first pass FSP, the IMCs exhibit a streamline distribution due to the combined effects of tool shoulder pressure and stirring pininduced fragmentation. This characteristic persists even after MFSP (Fig. 5(d-f)), despite an increased number of fine particles. In contrast, Fig. 5(g-i) reveals that DS-FSP leads to further refinement of IMCs and a significantly more uniform distribution. The overall quantity of IMCs appears reduced compared to single-sided FSP, which may be attributed to either partial dissolution during the DS-FSP process or the presence of ultrafine particles below the resolution limit of our observations.

To conduct a more detailed analysis of the size and morphology of IMCs in the DS-FSP alloy, Fig. 6 presents the distribution and elemental mapping of IMCs in the upper and middle regions of the SZ. In the upper region (Fig. 6a), IMCs exhibit a high degree of fragmentation and a nearly uniform dispersion, with sizes ranging from 2 to 4 μ m. This is due to the combined effects of shearing by the stirring pin and high axial pressure from the tool shoulder, which enhance particle refinement and homogenization. In contrast, in the middle

region (Fig. 6b), IMCs still show some streamline distribution, with larger particle sizes of 3 to 5 μ m. Fig. 6(c-d) provides a detailed view of region A in Fig. 6b, illustrating that the elemental composition of these particles remains consistent before and after DS-FSP, as confirmed by elemental mapping.

Fig. 7 summarizes tensile performances of the first pass FSP, MFSP and DS-FSP samples. As evident from Fig. 7a, the DS-FSP sample demonstrates higher values for both UTS and elongation compared to the one-sided FSP samples. Examining the trend of curves in Fig. 7a, it can be observed that the stress in one-sided FSP samples declines rapidly after reaching its peak, whereas the DS-FSP sample demonstrates a gradual decrease after reaching UTS, indicating that the sample underwent obvious necking. This behavior may be associated with crack propagation and strain accumulation [38]. The data results of mechanical properties are presented in Fig. 7b. The detailed data of the first pass FSP sample are UTS of 280.2 ± 28.2 MPa, YS of 140.3 ± 19.2 MPa and elongation of 18.4 \pm 4.3%, respectively. For the MFSP sample, the corresponding values are 311.4 \pm 20 MPa, 156.7 \pm 17.8 MPa and 21.8 \pm 6.3%, while those of the DS-FSP sample are 334.1 ± 15 MPa, 157.4 ± 12.7 MPa and $28.2 \pm 7.3\%$, respectively. Compared with the first pass FSP sample, UTS increased by 19.3% and elongation increased by 53.2%. Obviously, these results indicate that the DS-FSP method significantly contributes to tuning and enhancing the strengthductility.

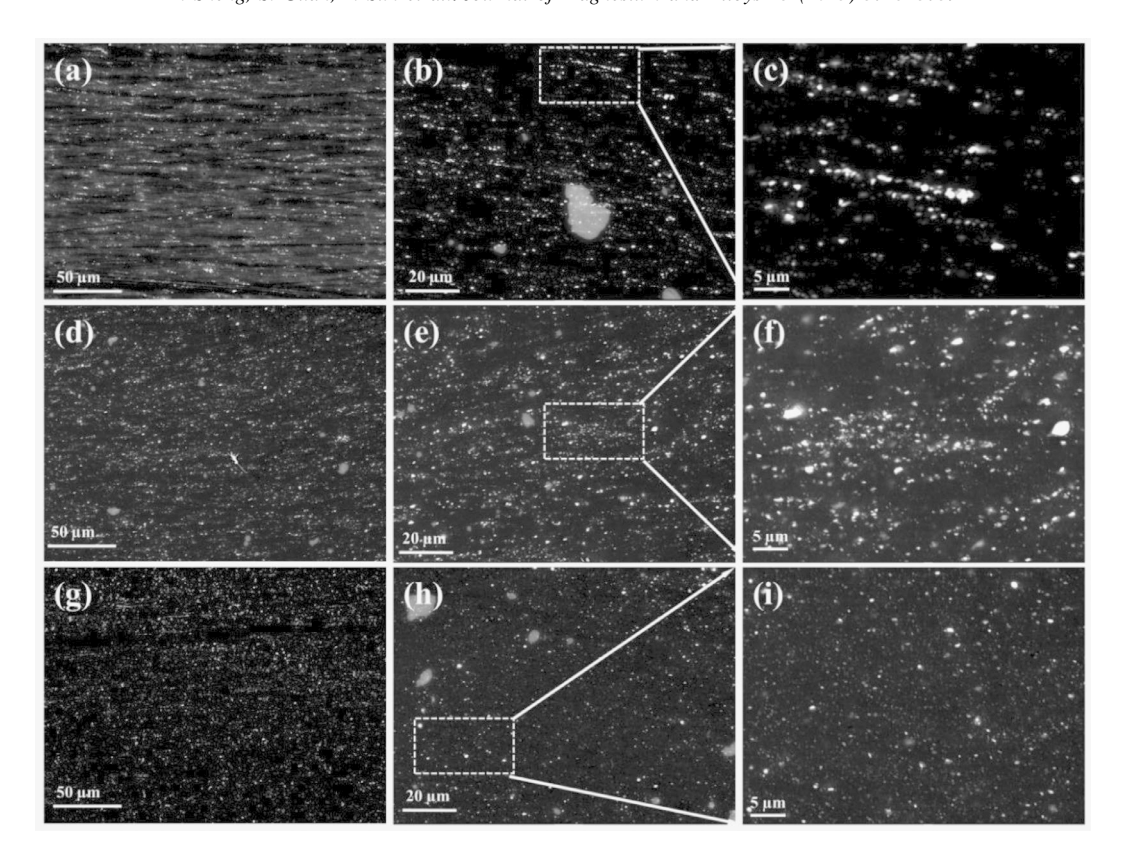


Fig. 5. IMCs distribution of the samples: (a-c) first pass FSP; (d-f) MFSP; (g-i) DS-FSP.

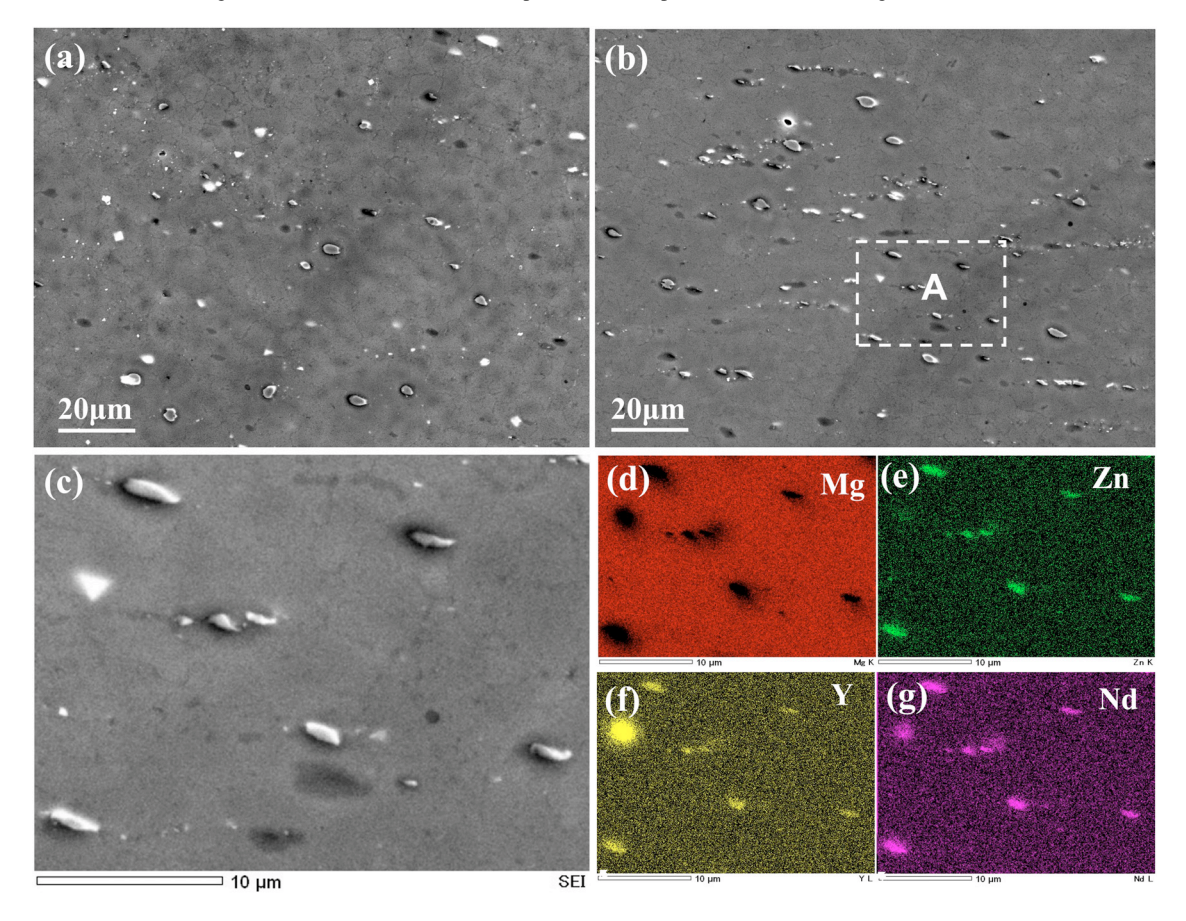


Fig. 6. Distribution of IMCs in the DS-FSP sample: (a) upper region of the SZ; (b) middle region of the SZ; (c) magnified view of region A in b; (d-g) elemental mapping of c.

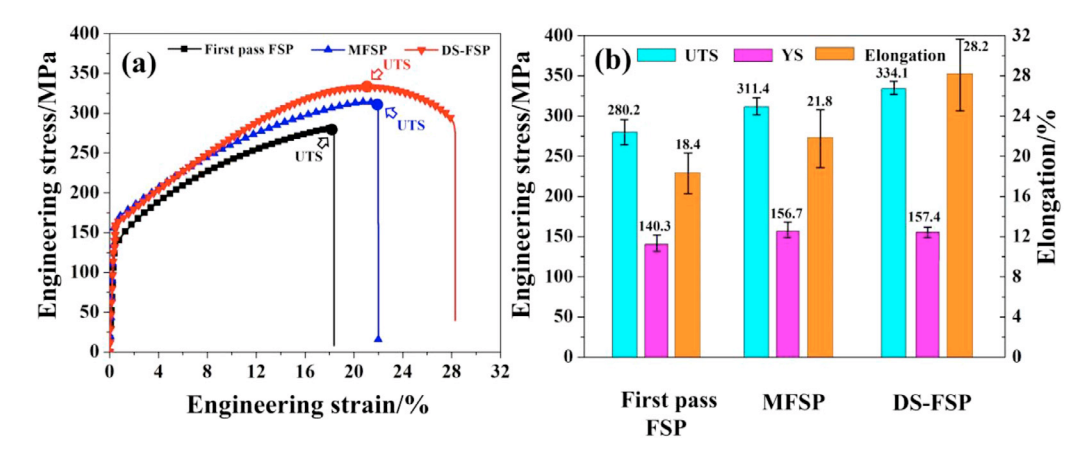


Fig. 7. (a) The stress-strain curves, and (b) data results of tensile performances of the first pass FSP, MFSP and DS-FSP samples.

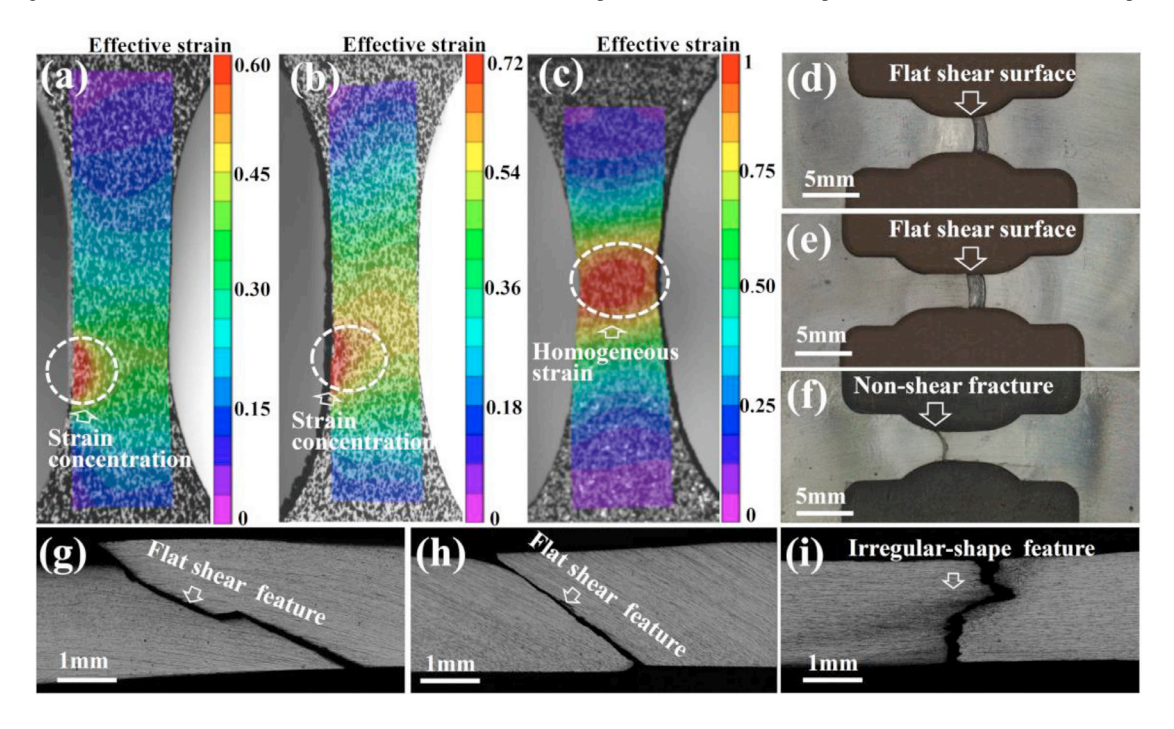


Fig. 8. The fracture fractured types of the first pass FSP, MFSP and DS-FSP samples: (a-c) the engineering strain distribution measured by digital image correlation, (d-f) fractured macro-graphs of the cross section, (g-i) fractured macro-graphs of the longitudinal section.

The engineering strain distribution maps of the first pass FSP, MFSP and DS-FSP samples measured by digital image correlation are shown in Fig. 8(a-c). For all samples, the fracture occurred in the range of gauge length. The values of accumulated effective strain are 0.6, 0.72 and 0.98, respectively. The DS-FSP sample exhibited the highest effective strain value. Moreover, strain concentration can be observed obviously in the first pass FSP and MFSP samples, while the DS-FSP sample shows homogeneous strain distribution and obvious necking, as shown in Fig. 8(a-c). Through a comparison of the microstructural characteristics and strain distribution between the one-sided FSP and DS-FSP samples, it can deduce that the homogeneous microstructure has the capacity to accumulate higher strain, resulting in a more uniform strain distribution. Fig. 8(d-e) shows the macro-graph of fractured the first pass FSP, MFSP and DS-FSP samples. The fracture surfaces exhibit two different fracture types: flat shear fracture and non-shear fracture. It can also be seen from the longitudinal section of the fractures that the one-sided FSP samples show relatively flat shear fractures in Fig. 8(g-h), while the fracture of the DS-FSP sample is irregular with some ridges and islands in Fig. 8i.

4. Discussion

By analysing the experimental results, the DS-FSP sample exhibits outstanding strength-ductility with irregular fracture, while the one-sided FSP samples show flat shear fracture. To elucidate the influence of microstructural characteristics on fracture behavior, the fractures are discussed in terms of initiation and growth, thereby clarifying the mechanisms be-

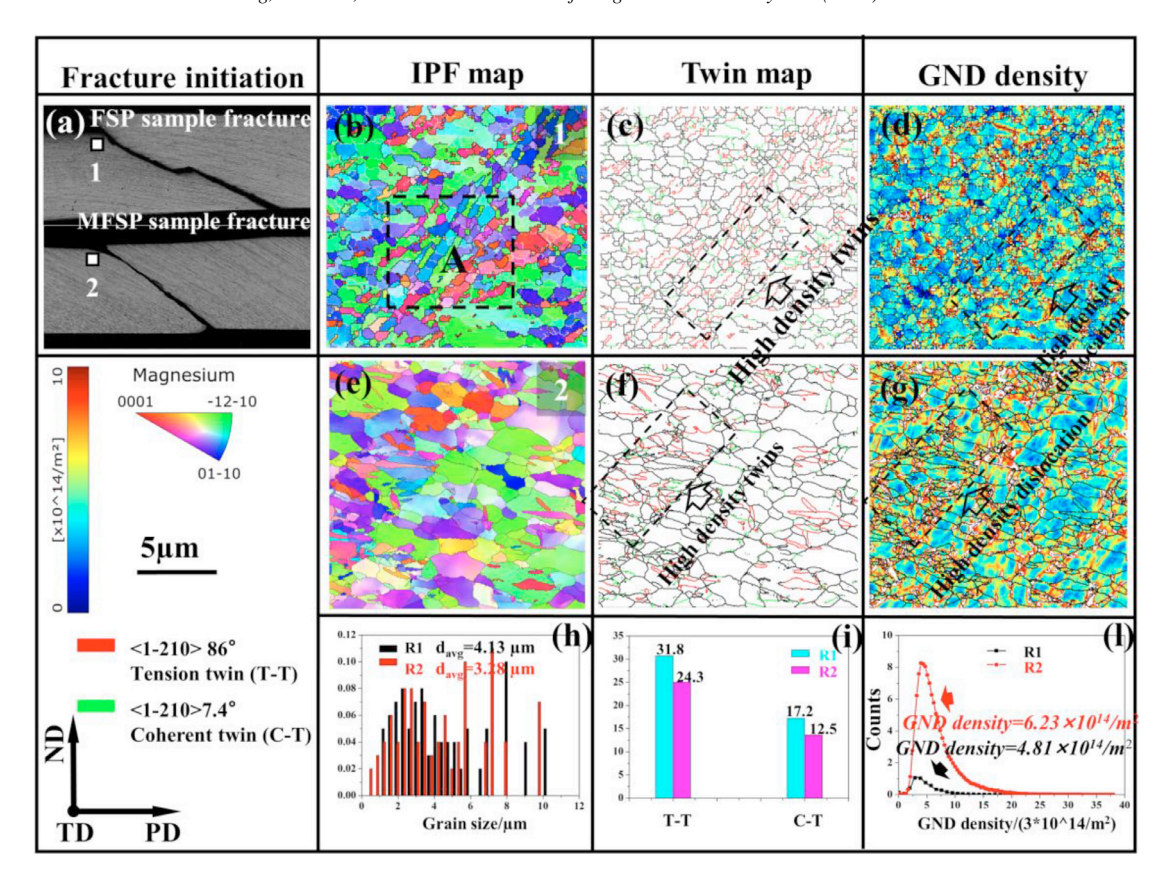


Fig. 9. (a) Fractures of the first pass FSP and MFSP samples, where regions 1, 2 are selected from the fracture initiation positions, (b) and (e) IPF maps, (c) and (f) twin distribution maps, (d) and (g) GND density maps, (h) grain size distribution histogram, (i) statistical histogram of T-T and C-T, (l) GND density distribution histogram.

hind the increased strength and ductility of Mg alloys through DS-FSP.

4.1. Fracture initiation of flat shear fracture of one-sided FSP samples

Fig. 9a shows the longitudinal section fracture morphology of one-sided FSP samples, both of them show obvious flat shear fracture. Regions 1 and 2 are selected at the fracture initiation for microstructure analysis. The grains are obviously elongated and numerous twins are evident in regions 1 and 2, as shown in Fig. 9b and 7e. From Fig. 9h, the grain sizes of regions 1 and 2 are about 4.13 µm and 3.28 µm, respectively. The twin distribution maps presented in Fig. 9c and 7f illustrate $\langle 1-210 \rangle$ 86° tension twins (T-T) and $\langle 1-210 \rangle$ 7.4° coherent twins (C-T), respectively. In Fig. 9i, the proportion of twins in region 2 is noticeably reduced compared to that in region 1, suggesting that the activation of twins is inhibited, possibly due to the refinement of grains [8,39]. During tensile deformation, the fine grains in one-sided FSP sample will generate twins, which play a role in coordinating deformation, resulting in a high local strain, which leads to fracture nucleation. For instance, Yu et al. showed that micro-cracks in single crystal Mg are initiated at twin boundaries and twin-twin interaction sites, where there is a localized stress concentration [40]. Moreover, the absence of stress relief for high local strain within twins leads to the development of micro-cracks, typically culminating in fracture [41,42]. Further extrapolating this result may be one of reasons for higher ductility of the MFSP sample compared to the first pass FSP sample.

To more precisely assess the impact of twinning on local strain, Fig. 9d and 9g depict distribution maps of geometrically necessary dislocation (GND) density. The GND densities are $6.23 \times 10^{14} \cdot \text{m}^{-2}$ and $4.81 \times 10^{14} \cdot \text{m}^{-2}$ in regions 1 and 2, respectively. Moreover, there are high GND density in the regions with high density twins, depicted in Fig. 9(c-d) and 9(f-g). Incidentally, GND density denotes the count of geometrically necessary dislocations per unit volume, distinct from conventional dislocation density, which encompasses the total dislocation count without regard to their distribution. The notion of GND density finds particular relevance in fine-grained or ultra-fine-grained materials characterized by diminutive dimensions, where non-uniform deformation notably influences the spatial arrangement of dislocation density [43,44].

Fig. 10(a-b) shows the TEM images at the fracture initiation position of the first pass FSP sample. The lamellar structures are well-maintained in certain regions, with clearly distinguishable boundaries between layers. At the same time, there is a notable variation in the distribution of linings within the lamellar structures, and the dislocations with high density are scattered throughout the dark regions depicted in

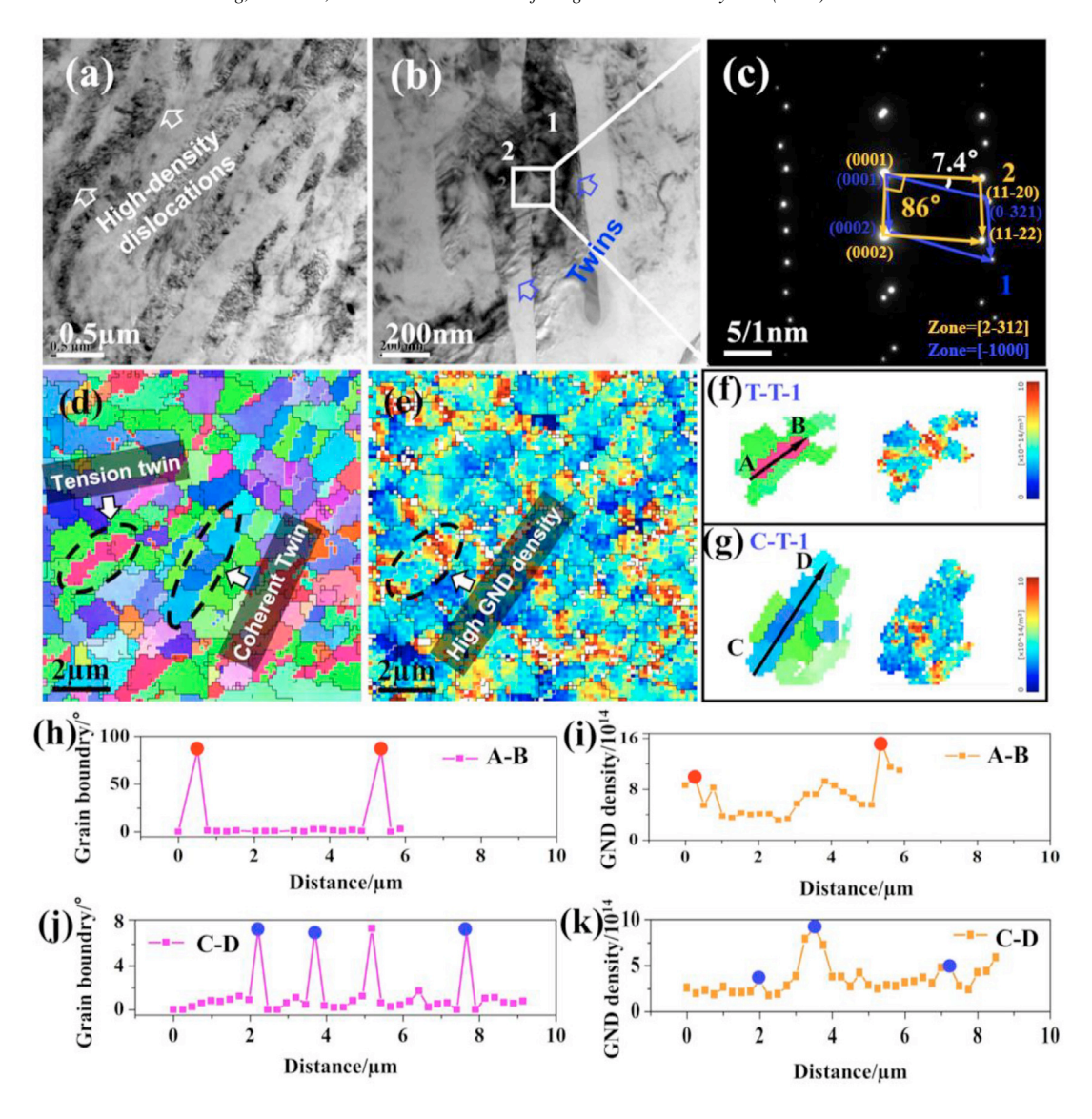


Fig. 10. Twins and dislocations characteristics at fracture initiation location of the first pass FSP sample: (a) TEM image, (b) local magnification image of a, (c) SAED of twin boundary, (d) IPF map A is selected in Fig. 9b, (e) GND density map; (f-g) T-T-1 and C-T-1 are selected in d, (h) and (j) grain boundary along A-B and C-D, (i) and (k) GND density along A-B and C-D.

Fig. 10a. In Fig. 10c, the selected area electron diffraction (SAED) result reveals the presence of twins at the interfacial boundary. A misorientation of 7.4° can be observed, suggesting an asymmetrical orientation in the twin structure [45]. EBSD maps corresponding to region A, as highlighted in Fig. 9b, are presented in Fig. 10d. By comparing Fig. 10(d-e), we can find that the region where the twins are located has a high dislocation density. To delve deeper into this result, we focus on T-T-1 and C-T-1 in Fig. 10(f-g), tension twins and coherent twins configurations are more prone to accumulating dislocations at the twin boundary. The lines in Fig. 10(f-g) point-to-point analyses were performed on T-T-1 and C-T-1, respectively. By comparing A-B and C-D grain boundary angle and GND density distribution, it can be found that the grain boundary angle corresponding to the twin is 86° and 7.4°, and the twin boundaries exhibit high dislocation density, as shown in Fig. 10(i-k).

4.2. Fracture growth of flat shear fracture of one-sided FSP samples

As depicted in Fig. 8, while both the first pass sample and MFSP sample exhibit a flat shear fracture, distinctions in the direction of fracture growth are evident. To elucidate the fracture growth mechanisms, the relationship between fracture behavior and microstructure is constructed in Fig. 11, where the tensile direction is the same as PD. From the schematic diagrams in Fig. 11a and e, the angles of fracture growth and tensile direction are 30° and 45° , respectively. Based on the shear fracture geometry, when θ is small, the predominant stress acting along the fracture direction is in the form of

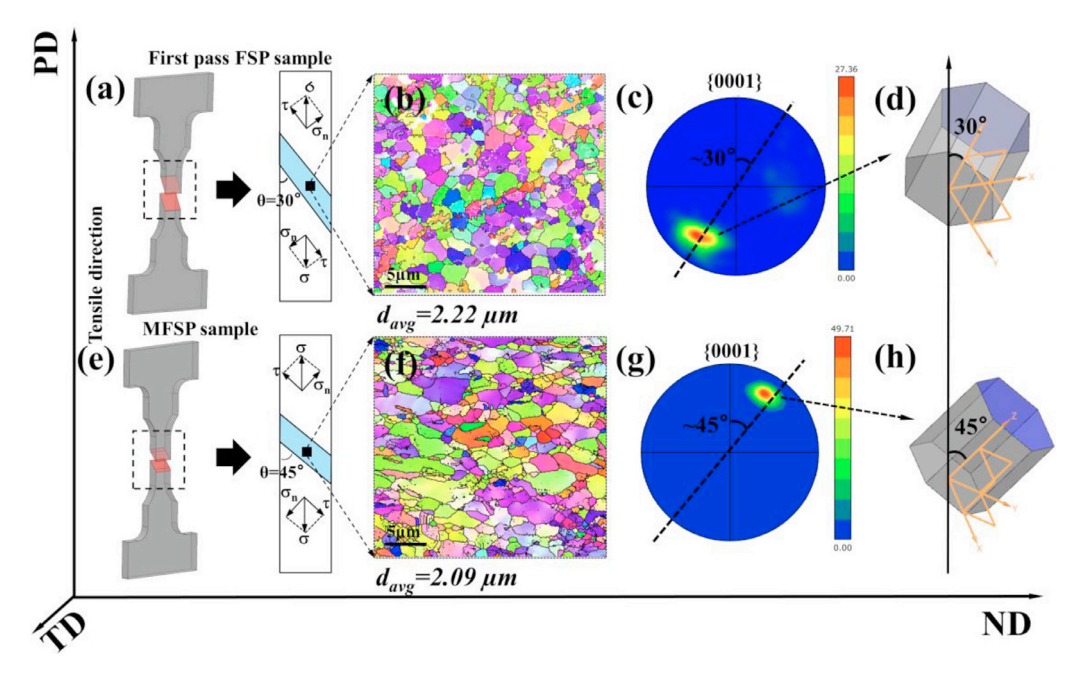


Fig. 11. (a) and (e) Schematic diagrams of the first pass FSP and MFSP samples tensile and fracture, (b) and (f) EBSD IPF maps at fracture growth locations, (c) and (g) {0001} pole figures at fracture growth locations, (d) and (h) crystal orientation of highest pole density points.

shear stress τ , making the material more susceptible to premature shear fracture. Therefore, it is essential to elucidate the reasons for the formation of the shear angle θ .

Fig. 11b and 11f show the EBSD IPF maps at locations where fracture growth occurred in the first pass FSP and MFSP samples, with average grain sizes of approximately 2.22 µm and 2.09 µm, respectively. Compared with fracture initiation locations (in Fig. 9b and e), the average grain size is smaller at fracture growth locations. From their corresponding {0001} pole figures, it can be found that the highest pole density points are tilted towards PD by about 30° and 45°, and the highest pole density are 27.36 mrd and 49.71 mrd, respectively. The texture of one-sided FSP samples has a strong density, which indicates that the texture has a high anisotropy in a certain direction. Incidentally, in the regions with high texture density, fracture may spread more easily along the texture direction. This is because the crystal orientations are relatively consistent in a specific direction, leading to lower resistance to crack propagation in that direction [46–48]. Therefore, the angles between the tensile direction and the z-axis of grain orientation are also about 30° and 45°. It could be inferred that the texture of fracture growth direction determines the direction of fracture growth.

4.3. Analysis of irregular fracture of DS-FSP sample

As mentioned earlier, the DS-FSP sample presents uniform strain distribution, and distinct irregular fracture at longitudinal section, not same as the shear fracture of one-sided FSP samples. Fig. 12 shows the microstructure characteristics of regions 1 and 2 at the fracture. Very few twins are observed in the EBSD IPF maps, which is obviously different from one-sided FSP samples. Micro-cracks with an irregular shape

are easily discernible in the band contrast map, as illustrated in Fig. 12b, resembling the macroscopic fracture depicted in Fig. 12g. Regions 1 and 2 in the fractured DS-FSP sample exhibit a higher GND density, with a more uniform distribution evident throughout, as depicted in Fig. 12c and f. The {0001} pole figures of regions 1 and 2 are shown in Fig. 12h and i, and the texture is tilted about 15° compared to texture of parallel TD before tensile testing. Due to strain loading during the tensile, there may occur changes in grain orientation, namely, rotation of grain orientation. This rotation may be attributed to behaviors like grain boundary sliding (GBS) or rotation [49–51]. The GND density are $8.18 \times 10^{14} \cdot \text{m}^{-2}$ and $8.19 \times 10^{14} \cdot \text{m}^{-2}$, as shown in Fig. 12j and k, respectively. Compared with the one-sided FSP samples, there are obvious differences in the microstructure of the fracture, and the dislocations have higher density and more uniform distribution, which could indicate the DS-FSP sample has more excellent strength and ductility.

From Fig. 13a, there are some high-density dislocations and equiaxed grains in the TEM image of the fractured DS-FSP sample, and no twins are observed. Fig. 13b is a local region magnification of Fig. 13a, where equiaxed grains can be clearly observed. This result is also mentioned in Zhang's report, which states that ultra-fine-grained Mg alloys still maintain equiaxed grains after tensile testing at ambient temperatures, primarily attributed to grain boundary sliding (GBS) as the principal deformation mode [52]. It is widely recognized that the deformation mechanisms in Mg alloys encompass twinning, dislocation slip, and GBS. Moreover, GBS is more easily activated in ultra-fine-grained Mg alloys than in coarse or fine grains. Compared to the generation of twins and dislocation slip during deformation, GBS can serve as a mechanism to release or relax stress and mitigate stress con-

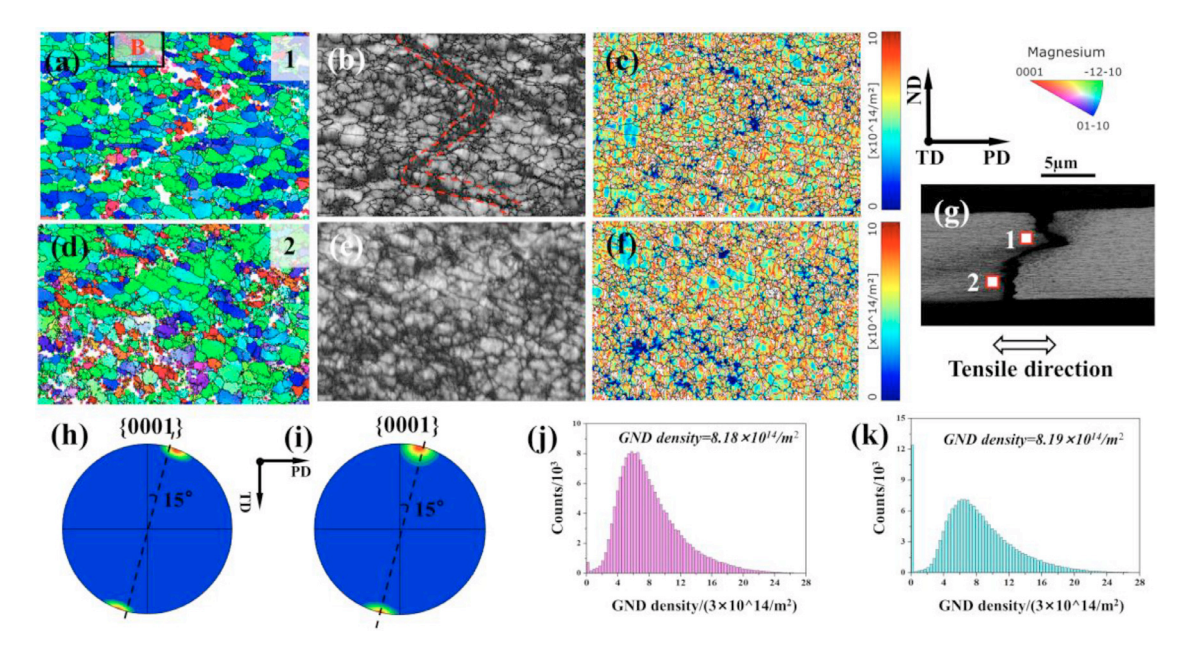


Fig. 12. Microstructure of region 1 and 2 in the fractured DS-FSP sample: (a) and (d) EBSD IPF maps, (b) and (e) band contrast maps, (c) and (f) GND density maps, (h) and (i) {0001} pole figures, (j) and (k) histograms of GND density distribution.

centration, thereby improving strength and ductility. As shown in Figs. 5 and 6, the refinement and homogenization of IMCs in DS-FSP samples also play a crucial role in promoting GBS. The reduced particle size and improved uniformity alleviate local stress concentration, facilitate more homogeneous deformation, and ultimately enhance both strength and toughness. However, GBS cannot be activated in all grains of the sample, and due to structural differences between different grains, local distortions may occur at grain boundaries, leading to strain concentration in these regions. This explains the presence of high-density dislocation regions and equiaxed grain regions in Fig. 13a.

In order to further clarify fracture initiation caused by structural differences between different grains, the region in Fig. 12a was selected and named B. From the band contrast and EBSD map (depicted in Fig. 13c), it is evident that region B (as shown in Fig. 12a) is situated in an area containing certain micro-cracks. Moreover, from Fig. 13c, the grain orientation at the micro-crack is significantly different from the adjacent grains. The grain boundary exhibits a high kernel average misorientation (KAM) value, as depicted in Fig. 13b, and this result may be related to activate GBS of ultra-fine grains. According to literature, when the stress concentration caused by grain boundary dislocation accumulation exceeds the critical level, the adjacent grains balance the stress distribution through GBS [53].

In Fig. 13e, the {0001} pole figure illustrates the orientations of the grains 1–4 (G1-G4), revealing a notable disparity in their orientations. Fig. 13f shows the grain orientation and tensile direction of G1, G2, G3 and G4 near the micro-crack, and the z-axis corresponding to crystal orientation is inconsistent with the tensile direction. Therefore, we can reasonably infer that, at the same deformation rate, due to different

shear stresses, they exhibit variations in the activation of slip systems, leading to changes in deformation among adjacent grains. Furthermore, the uncoordinated deformation among adjacent grains will cause uneven local deformation. Some relevant studies also proposed that the transfer of slip across grain boundaries serves as a crucial mechanism for hexagonal close-packed (HCP) metals to accommodate intergranular deformation incompatibility [54,55]. Moreover, owing to the two orders of magnitude difference in the critical resolved shear stress (CRSS) between the active basal and other slip systems, the primary slip system in magnesium is the basal slip system [19,56]. In order to study the relationship between crack generation and basal slip system activation, the lines of point-to-point are selected for analyzing basal slip system change in Fig. 13(g-i). Generally, it tends to be soft orientation when the Schmid factor (SF) value is >0.37, indicating that the basal slip system is easily activated [57]. Obviously, as depicted in Fig. 13(g-i), the SF values decrease from 0.45 to <0.37, indicating a change in the basal slip system of the grains along the lines from a soft orientation to a hard orientation near the micro-crack. That is, it can be inferred from Fig. 13 that GBS occurs in the ultra-fine-grained DS-FSP sample during the tensile testing, and variability in the activation capability of basal plane slip among adjacent grains influences slip transfer behavior, leading to the formation of micro-cracks.

Through a systematic analysis and discussion of the experimental results, we have established a schematic diagram depicting the microstructure characteristic and fracture behavior of one-sided FSP sample and double-sided FSP sample, elucidating the mechanisms behind enhanced strength and ductility, as depicted in Fig. 14. The schematic diagram consists of four parts: microstructure charac-

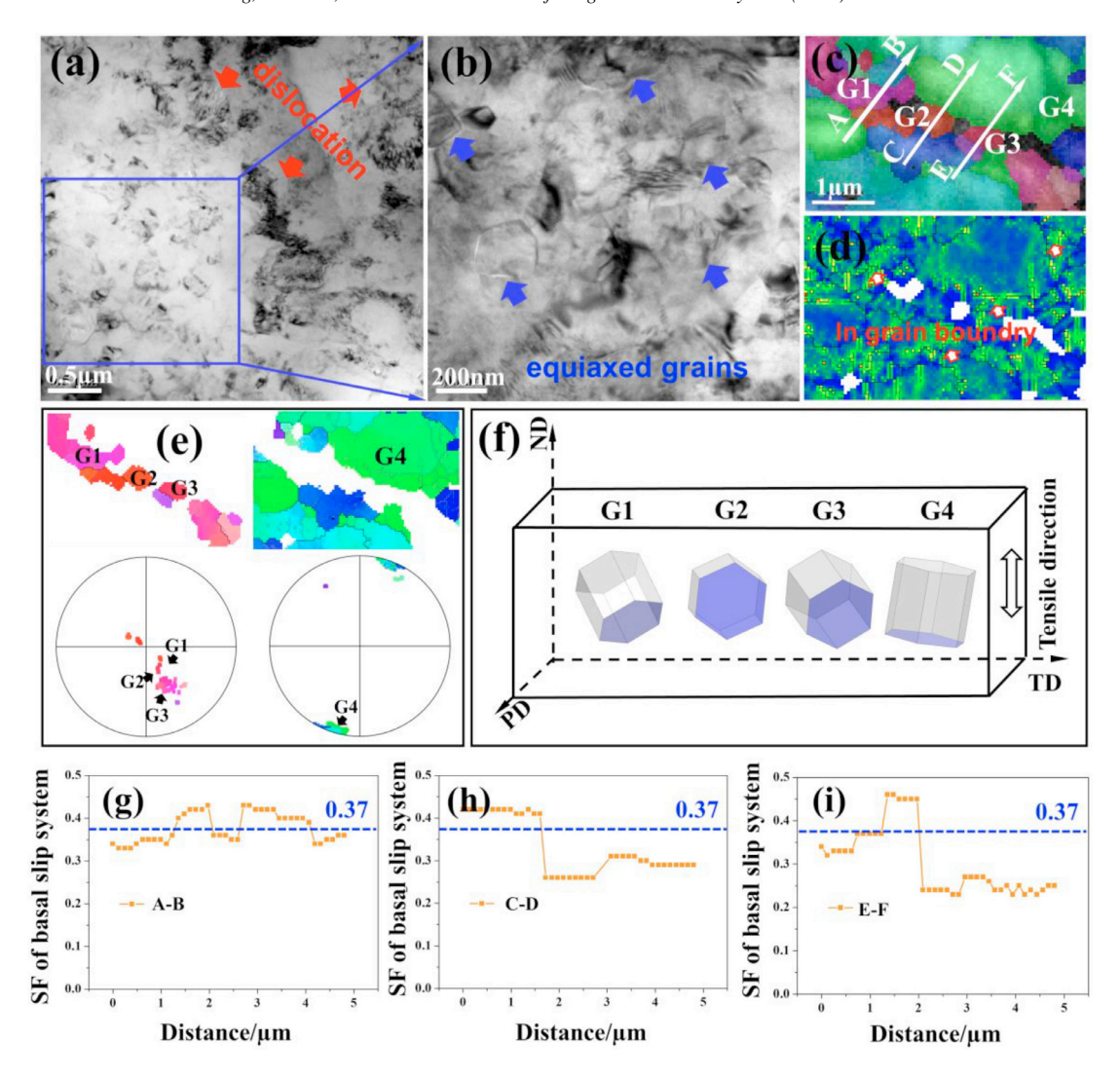


Fig. 13. TEM images of fracture initiation location of DS-FSP sample: (a) and (b) bright field image, (c) IPF map of the region B in Fig. 12a, (d) KAM map, (e) grains 1–4 are at the corresponding position of {0001} pole figures, (g) grain orientation and tensile direction of G1, G2, G3 and G4, (g-i) changes of SF along the lines.

teristics, fracture initiation, fracture growth and fracture morphology.

For the one-sided FSP sample, the microstructure is composed of heterogeneous and fine-grained grains, where the grain size at the fracture initiation area is larger than that at the crack growth area. According to the results shown in Figs. 9 and 10, T-T and C-T gradients are generated to coordinate the deformation of the sample, increasing the local GND density and leading to fracture initiation during the tensile processing. From the results presented in Fig. 11, due to the finer grain size in the fracture growth direction, a higher local GND density can be accumulated. Moreover, the fracture growth direction of the crack depends on the grain orientation along the growth path. The final fracture growth direction is at an angle of 30° or 40° to the tensile direction due to the strong texture present in the fracture growth direction of the sample, and the fractured sample exhibits a flat shear fracture morphology.

For the double-sided FSP sample, the microstructure is composed of ultra-fine grains, and there is no significant difference in grain orientation. Analysis of the results from Figs. 12 and 13 reveal that during tensile deformation, some grains in the ultra-fine grain sample undergo GBS, releasing local stresses, thereby leading to a decrease in local GND density. In the ultra-fine grain sample, smaller grain sizes may be more conducive to GBS. Hence, areas with relatively smaller grain sizes in Fig. 12 exhibit lower GND density. However, GBS may also alter grain orientation, causing the SF for basal slip to transition from a soft orientation to a hard orientation, resulting in deformation incompatibility between adjacent grains, thereby leading to the initiation of microcracks, ultimately resulting in irregular fracture morphology in the sample. It can be seen from the schematic diagram in Fig. 14 that compared with one-sided FSP sample, the ultra-fine grained double-sided FSP sample can accumulate higher GND density in the fracture initiation stage, which

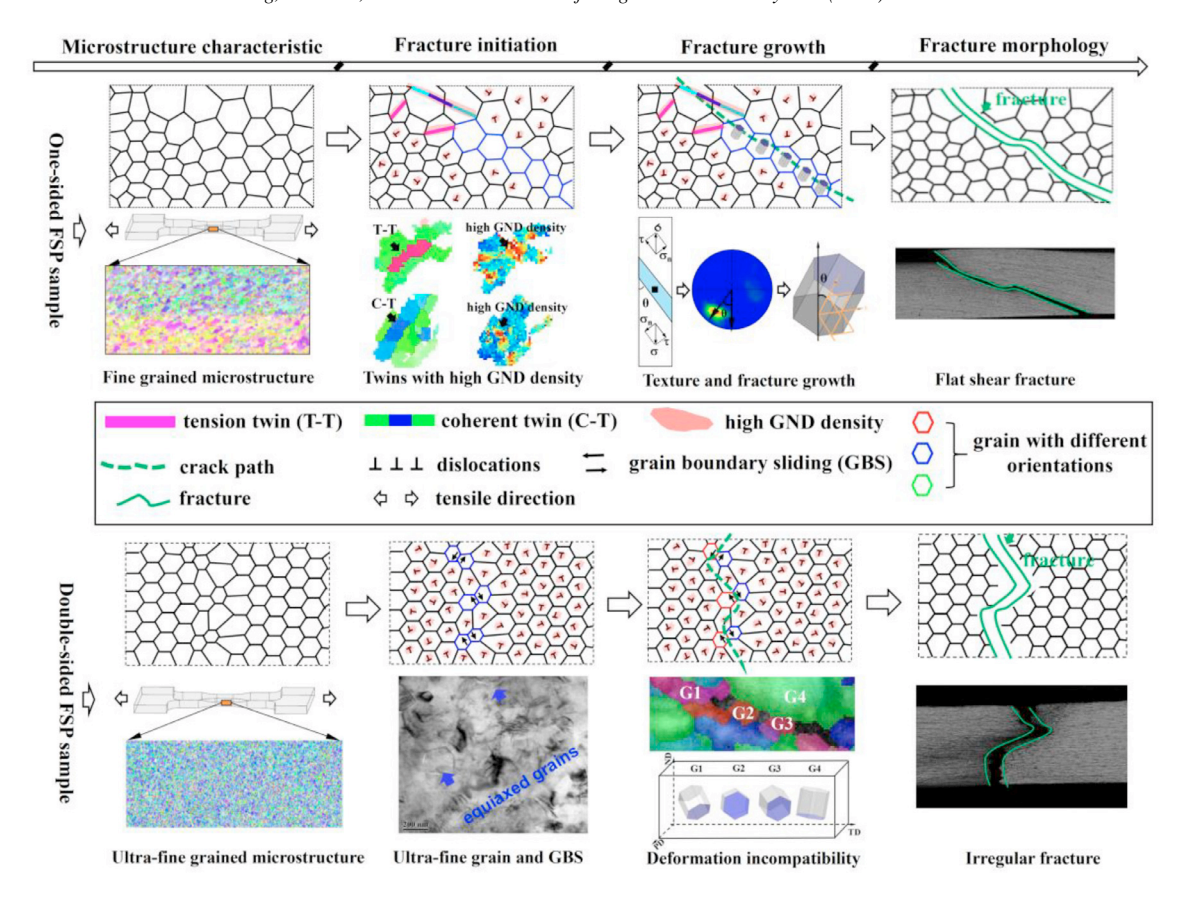


Fig. 14. Schematic diagram illustrating the influence of microstructural characteristics on fracture initiation, fracture growth, and fracture morphology during the tensile deformation.

improves the strength of the sample, and changes the fracture mechanism of the sample in the fracture growth stage, which improves the ductility of the sample. Simultaneously, double-sided FSP provides an effective strategy to change the fracture mechanisms by obtaining ultra-fine-grained and homogeneous microstructure, thereby enhancing the strength-ductility of bio-magnesium alloys.

5. Conclusion

Herein, we conduct a comprehensive investigation of one-sided and double-sided friction stir processing samples to deepen our comprehension of the relationship between strength-ductility and fracture mechanisms through analyzing microstructure and fracture behaviors. The following conclusions are obtained:

- (1) The ultra-fine-grained and homogeneous microstructure is manufactured via double-sided friction stir processing using liquid CO2 rapid cooling to enhance the strength-ductility of bio-magnesium alloy. The ultimate tensile strength and elongation of DS-FSP samples reach 334.1 ± 15 MPa and $28.2 \pm 7.3\%$, representing increases of 19.3%% and 53.2%, respectively, compared to first pass FSP sample.
- (2) DS-FSP fundamentally alters the fracture behavior of the processed magnesium alloy. The one-sided FSP

- samples exhibits a flat shear fracture morphology due to twin-induced high-density dislocation accumulation and a heterogeneous texture that constrains crack propagation. In contrast, DS-FSP samples show irregular fracture characteristics, attributed to GBS and variations in basal slip system activation between adjacent grains.
- (3) The ultra-fine-grained microstructure in DS-FSP samples facilitates GBS as the dominant deformation mechanism, reducing twin formation and enabling a more uniform strain distribution. This transition from twin-induced deformation in one-sided FSP to GBS-dominated deformation in DS-FSP effectively enhances both strength and ductility, as the higher dislocation density promotes work hardening while mitigating localized stress concentrations.

Declaration of competing interest

The authors assert that they do not have any identifiable competing financial interests or personal relationships that might have influenced the work presented in this paper.

CRediT authorship contribution statement

Kun Sheng: Writing – review & editing, Writing – original draft, Software. **Shaokang Guan:** Resources, Funding acquisition, Data curation, Conceptualization. **Yufeng Sun:**

Software, Methodology, Funding acquisition, Conceptualization. **Yoshiaki Morisada:** Supervision, Software, Resources, Conceptualization. **Hidetoshi Fujii:** Supervision, Resources, Project administration, Conceptualization.

Acknowledgments

Thanks for the financial support from the National Key Research and Development Program of China (2021YFC2400703), Zhengzhou City Major Special Project for Collaborative Innovation, and China Scholarship Council.

References

- [1] W.Q. Li, S.J. Zhu, Y.F. Sun, S.K. Guan, J. Alloys Compd. 835 (2020) 155369, doi:10.1016/j.jallcom.2020.155369.
- [2] K. Sheng, W.K. Li, P.H. Du, D. Mei, S.J. Zhu, L.G. Wang, S.K. Guan, J. Magnes. Alloy (2023), doi:10.1016/j.jma.2023.01.005.
- [3] J.Q. Zhou, L.N. Xin, D. Mei, F.L. Xue, C. Yan, P.H. Du, Y.F. Sun, J.F. Wang, S.J. Zhu, S.K. Guan, Mater. Sci. Eng. A 887 (2023) 145688, doi:10.1016/j.msea.2023.145688.
- [4] B. Che, L.W. Lu, J.L. Zhang, J.H. Zhang, M. Ma, L.F. Wang, F.G. Qi, Mater. Sci. Eng. A 832 (2022) 142475, doi:10.1016/j.msea. 2021.142475.
- [5] X.X. Qi, Y.X. Li, X.Q. Zeng, J. Alloy. Compd. 960 (2023) 170803, doi:10.1016/j.jallcom.2023.170803.
- [6] K. Sheng, L.W. Lu, Y. Xiang, M. Ma, Z.Q. Wu, J. Magnes. Alloy 7 (2019) 717–724, doi:10.1016/j.jma.2019.09.006.
- [7] D.J. Zhao, J. Qin, S.L. Lü, J.Y. Li, W. Guo, S.S. Wu, Y.H. Zhang, J. Mater. Process. Tech. 310 (2022) 117755, doi:10.1016/j.jmatprotec. 2022.117755.
- [8] S.K. Panigrahi, K. Kumar, N. Kumar, W. Yuan, R.S. Mishra, R.D. Lorme, B. Davis, R.A. Howell, K. Cho, Mater. Sci. Eng. A 549 (2012) 123–127, doi:10.1016/j.jmatprotec.2022.117755.
- [9] E.E. Klu, J.H. Jiang, G.W. Wang, B. Gao, A.B. Ma, D. Song, J. Mater. Res. Technol. 25 (2023) 3228–3242, doi:10.1016/j.jmrt.2023.06.108.
- [10] A. Rezaei, R. Mahmudi, R.E. Logé, J. Magnes. Alloy 10 (2023) 3815–3828, doi:10.1016/j.jma.2023.07.017.
- [11] H.R. Wu, J.H. Jiang, H. Liu, H. Huang, Y.H. Li, J.Y. Chen, A.B Ma, J. Mater. Res. Technol. 13 (2021) 1752–1758, doi:10.1016/j.jmrt.2021. 05 108
- [12] Z. Ruslan, V.G. Langdon, Prog. Mater. Sci. 51 (2006) 881–981, doi:10. 1016/j.pmatsci.2006.02.003.
- [13] G. Faraji, P. Yavari, S. Aghdamifar, M.M. Mashhadi, Mater. Sci. Technol. 31 (2015) 1879–1885, doi:10.1179/1743284715Y.0000000039.
- [14] J.B. Li, Q.D. Wang, J.Y. Chen, M.P. Liu, H.J. Roven, Trans. Nonferrous Met. Soc. China 20 (2010) 2081–2085, doi:10.1016/S1003-6326(09) 60421-0.
- [15] Q.D. Wang, Y.L. Mu, J.B. Lin, L. Zhang, H.J. Roven, Mater. Sci. Eng. A 699 (2017) 26–30, doi:10.1016/j.msea.2017.05.080.
- [16] M.T. Perez-Prado, J.A. del Valle, O.A Ruano, Scripta Mater 51 (2004) 1093–1097, doi:10.1016/j.scriptamat.2004.07.028.
- [17] H.J. Wu, F. Zhong, R.Z. Wu, Y. Wang, D. Wang, X.C. Ma, S.Y. Jin, S. Zhang, L.G. Hou, J.H. Zhang, Mater. Sci. Eng. A 859 (2022) 144199 ., doi:10.1016/j.msea.2022.144199.
- [18] V.C. Shunmugasamy, M. AbdelGawad, M.U. Sohail, T. Ibrahim, T. Khan, T.D. Seers, B. Mansoor, Bioact. Mater. 28 (2023) 448–466, doi:10.1016/j.bioactmat.2023.06.010.
- [19] M.R. Zhou, Y. Morisada, H. Fujii, J.Y. Wang, Mater. Sci. Eng. A 780 (2020) 139071, doi:10.1016/j.msea.2020.139071.
- [20] M.R. Zhou, Z.R. Zeng, C. Cheng, Y. Morisada, Q.Y. Shi, J.Y. Wang, H. Fujii, J. Magnes. Alloy. 10 (2022) 3064–3081, doi:10.1016/j.jma. 2021.12.002.
- [21] J. Chen, H. Fujii, Y.F. Sun, Y. Morisada, R. Ueji, Mater. Sci. Eng. A 580 (2013) 83–91, doi:10.1016/j.msea.2013.05.044.

- [22] M.V. Naik, N. Narasaiah, P. Chakravarthy, R.A. Kumar, J. Alloy. Compd. 970 (2024) 172160, doi:10.1016/j.jallcom.2023.172160.
- [23] A. Abdollahzadeh, B. Bagheri, M. Abbasi, F. Sharifi, A.O. Moghaddam, Surf Topogr-Metrol 9 (2021) 035038, doi:10.1088/2051-672X/ ac2176.
- [24] M. Abbasi, B. Bagheri, F. Sharifi, T. Nonferr. Metal. Soc. 31 (2021) 2626–2650, doi:10.1016/S1003-6326(21)65681-9.
- [25] B. Bagheri, M. Abbasi, A. Abdollahzadeh, S.E. Mirsalehi, T. Nonferr. Metal. Soc 30 (2020) 905–916, doi:10.1016/S1003-6326(20)65264-5.
- [26] B. Bagheri, A. Abdollahzadeh, M. Abbasi, A.H. Kokabi, Int. J. Mater. Form. 14 (2021) 623–640, doi:10.1007/s12289-020-01551-2.
- [27] S.H.C. Park, Y.S. Sato, H. Kokawa, Scripta Mater 49 (2023) 161–166, doi:10.1016/S1359-6462(03)00210-0.
- [28] Z. Nasiri, M.S. Khorrami, H. Mirzadeh, M. Emamy, Mater. Lett. 296 (2021) 129880, doi:10.1016/j.matlet.2021.129880.
- [29] Q. Liu, D.R. Ni, W. Wang, Y.T. Xiang, P. Han, T. Zhang, K. Qiao, F.M. Qiang, F.Q. Wang, K.S. Wang, Mater. Lett. 338 (2023) 134045, doi:10.1016/j.matlet.2023.134045.
- [30] H.P. Jia, K. Wu, Y. Sun, Mater. Today Commun. 31 (2022) 103526, doi:10.1016/j.mtcomm.2022.103526.
- [31] M. Elyasi, A. Razaghian, A. Moharami, M. Emamy, J. Mater. Res. Technol. 24 (2023) 4730–4742, doi:10.1016/j.jmrt.2023.04.104.
- [32] S.H.C. Park, Y.S. Sato, H. Kokawa, Scripta Mater 49 (2003) 161–166, doi:10.1016/S1359-6462(03)00210-0.
- [33] W.J. Yang, H. Ding, Y.L. Mu, J.Z. Li, W.J. Zhang, Mater. Sci. Eng. A 707 (2017) 193–198, doi:10.1016/j.msea.2017.09.028.
- [34] M. Raturi, A. Bhattacharya, Mater. Chem. Phys. 298 (2023) 127429, doi:10.1016/j.matchemphys.2023.127429.
- [35] X.Z. Han, L. Hu, D.Y. Jia, J.M. Chen, T. Zhou, S.Y. Jiang, Z. Tian, Trans. Nonferrous Met. Soc. China 33 (2023) 2351–2364, doi:10.1016/ S1003-6326(23)66264-8.
- [36] Y.B. Yang, J.X. Guo, C.Y. Wang, W.X. Jiang, Z.M. Zhang, Q. Wang, X. Zhang, J. Magnes. Alloy. (2023), doi:10.1016/j.jma.2023.01.018.
- [37] T. Al-Samman, G. Gottstein, Mater. Sci. Eng., A 488 (2008) 406–414, doi:10.1016/j.msea.2007.11.056.
- [38] Y.Q. Wang, Q. Yu, Y.Y. Jiang, Mater. Sci. Eng. A 831 (2022) 142193, doi:10.1016/j.msea.2021.142193.
- [39] J.Y. Kim, K.T. Yoo, J.W. Byeon, Mater. Character. 172 (2021) 110865, doi:10.1016/j.matchar.2020.110865.
- [40] Q. Yu, Y. Liang, J. Wang, Scr. Mater. 96 (2015) 41–44, doi:10.1016/j. scriptamat.2014.10.020.
- [41] M.R. Barnett, Sci. Eng 464 (2007) 1–7, doi:10.1016/j.msea.2006.12.037.
- [42] A.S.H. Mohamadi, M. Weiss, B.D. Arhatari, J. Adrien, E. Maire, M.R Barnett, Acta Mater 200 (2020) 619–631, doi:10.1016/j.actamat. 2020.09.016.
- [43] Q.E. Xie, Z. Lia, H.C. Ma, S. Liu, X.W. Liu, J.X. Liu, J.J Sidore, Mater. Sci. Eng. A 868 (2023) 144768, doi:10.1016/j.msea.2023.144768.
- [44] J.H. Zheng, C. Pruncu, K. Zhang, K.L. Zheng, J. Jiang, Mater. Sci. Eng. A 814 (2021) 141158, doi:10.1016/j.msea.2021.141158.
- [45] Y. Xu, X.X. Zhang, W. Li, P.H. Hu, J.B. Jia, J.T. Luo, Mater. Sci. Eng. A 781 (2020) 139221, doi:10.1016/j.msea.2020.139221.
- [46] H. Somekawa, T. Mukai, Scripta Mater 53 (2005) 541–545, doi:10. 1016/j.scriptamat.2005.04.048.
- [47] A. Abdollahzadeh, B.B. Vanani, A.M. Morghmaleki, Moghaddam AO Ahmad Ostovari, R.A Eivani, J. Compos. Mater 58 (2024) 2757– 2779, doi:10.1007/s13632-024-01117-7.
- [48] A. Abdollahzadeh, B.B. Vanani, H. Koohdar, A.A. Babereh, M. Yeganeh, Metallogr., Microstruct. Analys. 4 (2024) 13, doi:10.1007/ s12540-024-01670-4.
- [49] Y. Xiao, X.Y. Lan, Q. Liu, Y. Du, K. Li, Trans. Nonferrous Met. Soc. China. 33 (2023) 1655–1664, doi:10.1016/S1003-6326(23)66211-9.
- [50] A. Abdollahzadeh, B.B. Vanani, H. Koohdar, H.R Jafarian, Matal. Mater. Inter 30 (2024) 2830–2852, doi:10.1007/s12540-024-01670-4.
- [51] B.B. Vanani, A. Abdollahzadeh, J. Mater. Res. Technol 30 (2024) 6787–6801, doi:10.1016/j.jmrt.2024.05.066.
- [52] R.X. Zheng, W. Gong, J.P. Du, S. Gao, M.W. Liu, G.D. Li, T. Kawasaki, S. Harjo, C.L. Ma, S. Ogata, N. Tsuji, Acta Mater 238 (2022) 118243, doi:10.1016/j.actamat.2022.118243.

- [53] S. Amani, G. Faraji, H.K. Mehrabadi, J. Alloys Compd 723 (2017) 467–476, doi:10.1016/j.jallcom.2017.06.201.
- [54] B.J. Zhou, Y.J. Li, Wang LY, H.L. Jia, X.Q. Zeng, Acta Mater 227 (2022) 117662, doi:10.1016/j.actamat.2022.117662.
- [55] R. Ding, J. Gong, A.J. Wilkinson, I.P. Jones, Acta Mater 103 (2016) 416–423, doi:10.1016/j.actamat.2015.10.023.
- [56] S. Hidetoshi, W. Kota, K. Akihito, K. Akira, Mater. Sci. Eng. A 676 (2016) 427–433, doi:10.1016/j.msea.2016.09.014.
- [57] B. Che, L.W. Lu, Z.Q. Wu, H. Zhang, M. Ma, J. Luo, H.M. Zhao, Mater. Character. 181 (2021) 111506, doi:10.1016/j.matchar.2021.111506.